Snowfall retrieval at X, Ka and W bands: consistency of backscattering and microphysical properties using BAECC ground-based measurements

Marta Tecla Falconi[1], Annakaisa von Lerber[2], Davide Ori[3], Frank Silvio Marzano[1], and Dmitri Moisseev[2,4]

[1]Department of Information Engineering, Sapienza University of Rome, Italy and CETEMPS, L'Aquila, Italy
[2]Space and Earth Observation Center, Finnish Meteorological Institute, Finland
[3]Institute for Geophysics and Meteorology, University of Cologne, Cologne, Germany
[4]Institute for Atmospheric and Earth System Research / Physics, Faculty of Science, University of Helsinki, Finland

Correspondence to: Marta Tecla Falconi (martatecla.falconi@uniroma1.it)

Abstract. Radar-based snowfall intensity retrieval is investigated at centimeter and millimeter wavelengths using co-located ground-based multi-frequency radar and video-disdrometer observations. Using data from four snowfall events, recorded during the Biogenic Aerosols Effects on Clouds and Climate (BAECC) campaign in Finland, measurements of liquid-water-equivalent snowfall rate S are correlated to radar equivalent reflectivity factors Z_e, measured by the Atmospheric Radiation Measurement (ARM) cloud radars operating at X, Ka and W frequency bands. From these combined observations, power-law Z_e-S relationships are derived for all three frequencies considering the influence of riming. Using microwave radiometer observations of liquid water path, the measured precipitation is divided into light, moderate and heavy rimed snow. Interestingly light rimed-snow events show a spectrally distinct signature of Z_e-S with respect to moderate or heavy rimed-snow cases. In order to understand the connection between snowflake microphysical and multi-frequency backscattering properties, numerical simulations are performed by using the particle size distribution provided by the in-situ video-disdrometer and retrieved ice particle masses. The latter are carried out by using both the T-matrix method (TMM) applied to soft-spheroid particle models with different aspect ratios and exploiting a pre-computed discrete dipole approximation (DDA) database for rimed aggregates. Based on the presented results, it is concluded that the soft-spheroid approximation can be adopted to explain the observed multi-frequency Z_e-S relations if a proper spheroid aspect ratio is selected. The latter may depend on the degree of riming in snowfall. A further analysis of the backscattering simulations reveals that TMM cross-sections are higher than the DDA ones for small ice particles, but lower for larger particles. These differences may explain why the soft-spheroid approximation is satisfactory for radar reflectivity simulations, the errors of computed cross-sections for larger and smaller particles are compensating each other.

1 Introduction

Radar-based quantitative precipitation estimation (QPE) is a challenging task. To derive a relation between radar observables and precipitation rate knowledge of the particle size distribution (PSD) is required. For snowfall, this problem is compounded

by the uncertainty in ice particle microphysical and microwave scattering properties. Due to the large variability of snow particle properties (such as size, shape, density and fall velocity), snowfall QPE using radar measurements is more uncertain if compared to rainfall estimation (Matrosov, 1992; Rasmussen et al., 2003; von Lerber et al., 2017).

The relation between equivalent reflectivity factor, Z_e, and snowfall intensity, S, is usually assumed to follow a power-law form defined by two parameters, i.e. the prefactor a and exponent b. These parameters have been derived for weather radars operating in the centimeter wavelength range, either by using observations of radar reflectivity and snowflake size distribution (Gunn and Marshall, 1958; Sekhon and Srivastava, 1970; von Lerber et al., 2017), or by exploiting measurements of radar reflectivity values and coinciding data of snowfall rate (Boucher and Wieler, 1985b; Carlson and Marshall, 1972; Fujiyoshi et al., 1990a). The Z_e-S relationship applicable to mm-wavelength radars were derived in Matrosov (2007) and Matrosov et al. (2008). These studies have showed that cloud radars at Ka and W bands can be used to estimate snowfall accumulation and the vertical structure of snowfall rate (Mitchell, 1988).

Accurate snowfall retrieval algorithms using millimeter wavelengths are needed considering the increasing number of ongoing and planned satellite cloud and precipitation radar missions, and proliferation of ground observatories that operate mm-wavelength cloud radars, see for example Kollias et al. (2007) and Illingworth et al. (2007). The National Aeronautics and Space Administration (NASA) is currently operating the CloudSat (Stephens et al., 2002) mission carrying the W-band nadir pointing Cloud Profiling Radar (CPR). The NASA/JAXA Global Precipitation Measurement (GPM) core observatory has been launched in 2014 (Skofronick-Jackson et al., 2017) and carries the Dual-frequency (Ku and Ka-band) Precipitation Radar (DPR). Finally, the European/Japanese (ESA/JAXA/NICT) *EarthCARE* mission (Illingworth et al., 2015) is planned to be launched in 2019 and will carry a W-band Doppler radar on-board.

In Petty and Huang (2010), Botta et al. (2010) and Tyynelä et al. (2011) it was argued that for mm-wavelength radars the connection between scattering and microphysical properties of snowflakes is not as straightforward as was previously expected. It was presented that the use of soft-spheroid model, where ice particles are modeled as spheroids with dielectric properties derived from particle density using an effective medium approximation (EMA), may result in a significant underestimation of the radar cross sections. Kneifel et al. (2011) have demonstrated that deviations from the soft-spheroid particle model can be detected in the triple-frequency space, observations of which were reported by Leinonen et al. (2012) and Kulie et al. (2014). Kneifel et al. (2015) have shown that the soft-spheroid particle model tend to fail in cases where large low-density aggregates are observed. Given the mounting body of evidence that the relatively simple soft-spheroid models may not be capable of capturing the complexity of ice particle and therefore establish the link between physical and scattering particle properties, the applicability of the Z_e-S relationships derived for mm-wavelength radars needs to be re-evaluated.

To address this topic, the present study aims to establish and evaluate Z_e-S relations at X, Ka and W bands by combining the multi-frequency radar measurements and collocated ground observations. The presented dataset is collected during the BAECC measurement campaign that took place at the University of Helsinki research station in Hyytiälä, Finland (Petaja et al., 2016). Four snowfall cases, comprising of various snowfall regimes and snow microphysical properties, are analyzed. In order to check whether the derived multi-frequency Z_e-S relations can be explained by using soft-spheroid particle models, scattering simulation using TMM and DDA were carried out. Observations from video disdrometer, Particle Imaging Package

(PIP) (Newman et al., 2009; Tiira et al., 2016), were used to constrain these scattering computations. The PIP measures PSD, particle dimensions and fall velocities (Tiira et al., 2016). From these observations particle masses were derived (von Lerber et al., 2017) using the hydrodynamic theory (Böhm, 1989; Mitchell and Heymsfield, 2005). Given particle dimension and mass, corresponding scattering properties were retrieved from a scattering database (Leinonen and Szyrmer, 2015) or equivalent refractive index was computed using Maxwell Garnett EMA (Sihvola, 1999) and applied to TMM scattering computations. From the computed equivalent radar reflectivity factors and measured snowfall rates, Z_e-S relations were derived and compared against the previously retrieved radar-based relations.

This paper is organized as follows. The BAECC campaign setup, including an analysis of the calibration and attenuation corrections applied to radar measurements, is given in Section 2. The methodology, used to derive Z_e-S relationships from empirical measurements and the details about the single-scattering computations, are described in Section 3. Results from the field observations and numerical analysis are shown and discussed in Section 4. Section 5 draws final conclusions and remarks.

2 Measurements and data

In 2014 the University of Helsinki Hyytiälä Forestry Field Station hosted an 8-months measurement campaign, BAECC (Petaja et al., 2016). BAECC was jointly organized by the University of Helsinki (UH), the U.S. Department of Energy ARM program, the Finnish Meteorological Institute (FMI) and other international collaborators. During the main campaign, the snowfall intensive observation period (BAECC SNEX IOP) took place between 1 February and 30 April 2014. It was carried out in collaboration with the NASA GPM ground validation program (Petaja et al., 2016). BAECC SNEX IOP focused on surface observations of snowfall microphysical properties in combination with multi-frequency radar measurements to establish a link between physical and scattering properties of ice particles. In this study observations of this IOP are used. The surface-based snowfall measurements were carried out by the PIP and a weighing precipitation gauge OTT Pluvio^2. The AMF2 two channel MWR measurements were used to classify the data into three riming classes using the retrieved LWP (Cadeddu, 2014; Moisseev et al., 2017). The multi-frequency radar observations were obtained by the X-band scanning ARM cloud radar (XSACR), Ka-band ARM zenith radar (KAZR), and the Marine W-band ARM cloud radar (MWACR), which were part of the AMF2 deployed at the measurement site during BAECC. In addition to these radars, an operational C-band dual-polarization Doppler weather radar of Finnish Meteorological Institute (FMI) is utilized as a reference in the cross-calibration of the ARM radars, as discussed below.

2.1 Surface precipitation measurements

The video-disdrometer PIP measures hydrometeor size, fall velocity, an estimate of particle shape and PSD. In this study PIP data are used for characterizing the microphysical properties of the snowfall, which include estimates of the mass-dimensional $m(D)$ relations. The PIP instrument works in the same way as its predecessor, the Snow Video Imager (SVI) (Newman et al., 2009), but using a camera with a higher frame rate of 380 frames per second. The 2D-gray scale images of falling particle are obtained, when it falls between the camera and the lamp (distance between the two is 2 m) and from these multiple images

the particle fall velocity is derived. The camera focal plane is at 1.3 m and the field of view is 64×48 mm with a resolution of 0.01 mm^2. Sampling volume of PIP depends on particle size and fall velocity (Newman et al., 2009). For each particle, the PIP processing software automatically records the disk-equivalent diameter D_{Deq}, which is the diameter of a disk with the same area as the particle shadow.

Particles smaller than 14 pixels (approximately $D_{Deq} < 0.2$ mm) or particles only partly observed or out of focus (blurred) are rejected by the software (Newman et al., 2009). Because of the blurring effect, the sizing standard error is estimated to be 18% (Newman et al., 2009). Also, other shape-descriptive particle parameters are retrieved with the image processing software (National Instruments IMAQ) such as particle orientation, total area, and bounding box width and height. Particle fall velocities are recorded as a function of D_{Deq} and values are considered reliable, if there are more than two observations of the identified particle and values are higher or equal to 0.5 ms^{-1} (PIP software release 1308). In later software versions the fall velocity threshold is removed. The PIP dataset includes PSD in m^{-3}mm^{-1} for every minute. It is also determined as a function of D_{Deq} and subdivided into 105 bins (from 0.125 to 25.875 mm) with the last bin containing particles larger than 25.875 mm. The observed maximum diameter D_{max} for each particle is determined by fitting an ellipse inside the bounding box with considering the particle orientation angle as explained in von Lerber et al. (2017), and the mean ratio between D_{max} and D_{Deq} is approximately 1.38. For simplicity, D will be used hereinafter to replace D_{Deq}.

In this study 5-minute time series of the observed PSD, the fitted $v(D)$ and the retrieved $m(D)$ relations are utilized (Tiira et al., 2016; von Lerber et al., 2017) as a function of the diameter D. Typically during the 5-minute period 10^3 particles are observed. The PSD is averaged from one minute observations, after spurious particle records are filtered out. The $v(D)$ relation is derived by a linear regression fit in the log-space for the observed particles during every five minutes (Tiira et al., 2016). The $m(D)$ relation is retrieved by utilizing the general hydrodynamic theory (Böhm, 1989; Mitchell and Heymsfield, 2005), where a snow particle mass is computed from the observed dimension, fall velocity and area ratio of a snow particle. The PIP observes falling particles from the side, whereas the particle dimensions projected to the flow are needed for the hydrodynamic calculations. In von Lerber et al. (2017), errors associated with the observation geometry, and also with the measured PSD were addressed by devising a simple correction procedure; the value of the correction was chosen for each snow event by comparing the estimated liquid water equivalent (LWE) accumulation to precipitation gauge measurements. Similar to $v(D)$ relation, the power-law $m(D) = a_m D^{b_m}$ fit is determined by a linear regression fit in the log-space for the computed particle masses every five minutes. The uncertainty in the retrieved factors of $m(D)$ relation are discussed in detail in von Lerber et al. (2017).

The weighing precipitation gauge, OTT Pluvio^2 200, records every minute the bucket weight expressed in millimeters. The gauge is located on a platform at 2 m height surrounded by a double wind fence similar to Double Fence Intercomparison Reference (DFIR)-fence (Goodison et al., 1998). In addition, the gauge has a Tretyakov wind shield. The Hyytiälä measurement site is surrounded by boreal forest, and therefore, the wind effects are usually moderate. The PIP measurement volume is open and typically affected less by the wind than instruments with enclosed sampling volumes (Nešpor et al., 2000). Therefore, in these wind conditions, the expected wind induced errors are expected to be small.

2.2 AMF2 two-channel MWR

The AMF2 two-channel MWR, located $20\ \mathrm{m}$ away from PIP, is a sensitive microwave receiver that provides time-series measurements of column-integrated amounts of water vapor and liquid water. Two channels, respectively $23.8\ \mathrm{GHz}$ and $31.4\ \mathrm{GHz}$, allow to obtain simultaneously water vapor and liquid water along line of sight (LOS) path. The LWP is estimated on a weighted difference of the optical thicknesses of the two channels. In von Lerber et al. (2017) the LWP was used as a proxy of riming, and in this study we use the LWP as the driven observable for the k-means clustering of the dataset.

2.3 Ikaalinen C-band weather radar

The Ikaalinen dual-polarization Doppler weather radar (IKA), used for cross-calibration analysis, belongs to the Finnish weather radar network (Saltikoff et al., 2010). It operates at C-band and is located circa $64\ \mathrm{km}$ west of Hyytiälä. The antenna has an half-power beam widths of 1°. The radar performs volume scans, repeated every 5 min, and range height indicator (RHI) scans over the Hyytiälä site every 15 min.

The IKA data is quality controlled and calibrated using a number of techniques. The engineering calibration, where different radar components are characterized, is performed during the radar installation and after major system modifications (Saltikoff et al., 2010). In addition to the engineering calibration, the radar receiver and antenna pointing are monitored using sun observations (Huuskonen and Holleman, 2010). The differential reflectivity calibration is monitored using a combination of vertically pointing scans and sun observations. During the summer months, the IKA radar absolute calibration was checked using the polarimetric self-consistency principle (Gorgucci et al., 1992; Gourley et al., 2009).

Given the continuous monitoring of the radar stability and regular calibration, we use the IKA observations as the calibration standard for the ARM radars. This approach allows us to cross-calibrate the ARM radars even in presence of radome attenuation caused by e.g. large snow accumulation.

2.4 ARM cloud radar system calibration at X, Ka and W band

The ARM cloud radar systems operating at X, Ka and W band are integral part of the BAECC snowfall IOP. The antennas of the XSACR, X-band scanning ARM cloud radar, and KAZR, Ka-band ARM zenith radar, are mounted on top of two containers located $17\ \mathrm{m}$ away from each other. The MWACR, marine W-band ARM cloud radar, is mounted on the same container as KAZR. All the ARM radars make zenith-pointing observations. Looking at the radar technical properties in Table 1, the range gate spacing and the temporal sampling are comparable, but there is a difference in the beam width between XSACR and the other two systems. To reduce the beam mismatch and to facilitate the intercomparison with the ground-based sensors, all the radar data are averaged to 5-minutes. To derive consistent X-, Ka- and W-band Z_e-S relations, the measured radar reflectivity factors were calibrated and corrected for attenuation. The absolute calibration of ARM cloud radars has been performed at the beginning and during the BAECC IOP using engineering calibration and external standard target procedure.

We have also performed a cross-calibration in order to reduce biases between different radar systems. The cross-calibration method is based on the assumption that in the low reflectivity region at the cloud top the small crystals basically scatter in

the Rayleigh regime (Hogan et al., 2000). We have compared the radar measurements in regions close to cloud top (height higher than 5 km) in non-precipitating ice clouds. The selected radar reflectivity profiles had to have reflectivity values of less than 0 dB. Furthermore, only cases where no lower clouds or precipitation were detected were used for calibration. The cross calibration was performed for all the cases before and after the snowfall events. Only events where the cross-calibration values did not change are used in this study. As mentioned in Section 2.3, the IKA radar observations are considered to be the reference for this analysis. The main reason for this selection is that the IKA radar is very stable and its performance is well-monitored. Additionally, given its operating frequency it does not suffer from attenuation during winter storms. Figure 1 (a) shows the profile of 15 February 2014 at 17:13 UTC in which we performed the calibration between 4 and 6 km and in Figure 1 (b) the histograms of the three different calibration errors. The calibration error, measured as the standard deviation of the histograms in Figure 1 (b), shows that the best result is for the error between Ka- and W-band and the worse is for C- and X-band, this being related mostly to the beam width. Looking at Table 1 larger is the beam width greater is the measured dispersion and vice versa.

One of the reasons for differences in reflectivity measurements can be also attributed to the radome attenuation. For example, the flat shape of the KAZR radome increases the possibility of heavy snow accumulation during a storm. Consequently, when the temperature goes beyond the melting point of ice, the melting snow could produce heavy attenuation that should be monitored. On the other hand, the conical shape of the MWACR radar limits the amount of accumulated snow, but because of the higher operating frequency is more sensitive to the freezing rain/drizzle. To monitor the radome attenuation sky-noise analysis has been performed for the millimeter-wavelengths radars, KAZR and MWACR. The sudden changes in the sky-noise temperature can be resulted from the increased surface temperature, which may indicate snow melting, and thus increased radome attenuation. The data in these cases are discarded. The stability analysis made with the sky noise is shown in Figure 2 as a histogram of sky-noise power measured during ten snowfall days of BAECC IOP. The standard deviations is around 0.25 and 0.14 dBm respectively for KAZR and MWACR radar; according to these values, cases during the ten snowfall events are excluded from the cross-calibration. This is shown in the Ka-band histogram in Figure 2, where a secondary Gaussian-like peak is visible centered around -68.06 dBm.

During the BAECC IOP, radiosondes were launched four times a day. Using these observations as the input to the millimeter-wave propagation model (Liebe, 1985), the two-way gaseous path attenuation was computed for the dataset. This computation has been performed for all the dataset. For example, for 15 February 2014 at 17:24 UTC, the Ka-band the two-way gas attenuation is 0.4334 dB. For the same time sample, the W-band two-way gas attenuation is 1.0206 dB. As expected, the attenuation for the W-band is about twice as large as for Ka-band. By taking into account the gaseous attenuation, the radar calibration offsets during the snowfall experiment were estimated as 2.9 dB for the XSACR, 3.9 dB for the KAZR and 4 dB for the MWACR. The results shown for the case study of 15 February 2014 have also been checked for other snow events inside the dataset confirming the consistency of the calibration analysis.

3 Methods

The focus of this study is to investigate the consistency of Z_e-S relations at different frequencies, namely at X-, Ka- and W-band. Given the current discussion on scattering properties of ice particles at millimeter wavelengths (Kneifel et al., 2018), the derived multi-frequency Z_e-S relations are used to test the soft-spheroid model and compared with DDA scattering simulation.

3.1 Deriving Z_e-S relations at X, Ka and W band

The equivalent reflectivity factor Z_e, measured by the radar systems at different wavelengths, and the liquid-water-equivalent snowfall rate S, evaluated from PIP, are the two related variables. The S (in $\mathrm{mm/h}$) is derived from mass flux as

$$S = \frac{3.6}{\rho_w} \int m(D)v(D)N(D)dD, \tag{1}$$

where m is the mass (in g), v is the velocity (in $\mathrm{m/s}$) , N is the particle size distribution (PSD, in $\mathrm{mm^{-3}m^{-1}}$) and ρ_w is the liquid water density (in $\mathrm{gcm^{-3}}$). In (1) all quantities are expressed in terms of the disk-equivalent diameter $D = D_{Deq}$ and derived from PIP measurements (von Lerber et al., 2017).

The radar data used in this study were collected in the vertical pointing mode. To match radar and in-situ measurements, the radar data at the lowest meaningful altitude were used. Given the different radar specifications, see Table 1, the Fraunhofer far-field distance for the radars is different. This distance defines the near-field of the radars and is related to the radar antenna size. The beam width difference is related to the antenna diameter that is respectively for XSACR, KAZR and MWACR, 1.82; 1.82; 0.9 m so that the Fraunhofer distance ($2D^2/\lambda$) is approximately 214 m for XSACR, 773 m for KAZR and 514 m for MWACR. Taking into account the near-field influence, all radar data are selected at 400 m (Sekelsky, 2002).

Another important aspect is related to the different time acquisitions for the various instruments. In Table 1 we note that the temporal sampling of the radars is 2 s whereas for the PIP instrument is 1 min. To ensure similar sampling, we have decided to average data over 5 min. This results in PIP sampling volume of roughly 1 $\mathrm{m^3}$ for ice particles falling with fall velocity of 1 $\mathrm{m/s}$. As mentioned in Section 2, the averaging is also useful to tackle the differences in radar beam widths.

The Z_e-S is expressed in a power-law form, $Z_e = aS^b$, where Z_e is in $\mathrm{mm^6m^{-3}}$ and S is in $\mathrm{mm/h}$ (Carlson and Marshall, 1972; Matrosov et al., 2008). In order to estimate the regression coefficients, we can choose a non-linear least squares in the variable linear space or a linear least squares in the log-log variable space. We have adopted the latter approach by applying a linear regression as in Boucher and Wieler (1985b). The applied log-log model is given by:

$$log_{10} Z_e = b \log_{10} S + \log_{10} a. \tag{2}$$

where Z_e can be either the time-averaged range-resolved co-polar radar measurement (disregarding the near-field effects) or the numerically simulated backscattering radar response.

3.2 Multi-frequency Z_e-S relations using T-matrix scattering model

Single scattering computations for spheroids are performed using Python implementation (Leinonen, 2014) of the TMM code (Mishchenko, 2000). The spheroidal particle model has been widely used for describing raindrops, but also approximating

more complex particles such as snowflakes (Matrosov, 2007; Dungey and Bohren, 1993). In this study the spheroid model is initiated by using retrieved snowflake masses and maximum dimensions. This leaves the spheroid aspect ratio as a free parameter that adjusts volume, density and therefore the refractive index.

The aspect ratio is defined as $r_s = b_s/a_s$ where a_s and b_s are the horizontal and vertical dimensions of the spheroid ($r_s = 1$ spherical particle, $r_s \geq 1$ prolate particle and $r_s \leq 1$ oblate particle) (Dungey and Bohren, 1993). The snowflakes, due to aerodynamic forcing, typically fall with the major axis preferentially oriented horizontally (Magono and Nakamura, 1965; Matrosov, 2007). We have modeled the spheroids preferentially horizontally oriented with 10° standard deviation of the canting angle distribution following Matrosov (2007) and Matrosov et al. (2008). It should be noted that while snowflakes in the nature may have wider orientation angle distributions, the goal of the particle models used for scattering computations is to provide a link between radar observation and cloud/precipitation properties such as snowfall intensity or ice water content. This goal does not necessary imply that all of the particle model properties coincide with properties of naturally occurring snowflakes. Our studies show that use of wider canting angle distributions results in worse agreement between measured and computed radar reflectivity values (Tyynelä et al., 2011).

To test whether the spheroidal model can produce consistent multi-frequency radar observations, the TMM computations are performed using different aspect ratios. If the computations with the same aspect ratio value can explain measured Z_e - S relations at all the frequencies, then spheroidal model can be considered adequate. If different aspect ratios are needed, then the model has failed. As stated-above, the aspect ratio defines particle density as:

$$\rho = \frac{m}{\pi/6 D_{Veq}^3} \tag{3}$$

in which the mass m is defined as in von Lerber et al. (2017) and D_{Veq} is the volume equivalent diameter defined from D_{max}, the maximum diameter obtained by PIP (von Lerber et al., 2017), as $D_{Veq} = r_s^{1/3} D_{max}$. The presence of the aspect ratio inside the density reflects its influence on the complex refractive index of snow m_S that is defined through the Maxwell Garnett EMA.

The Γ-size distribution (in $\mathrm{mm}^{-1}\mathrm{m}^{-3}$) is assumed to model the PSD:

$$N(D_{Veq}) = N_{w,Veq} f(\mu_{Veq}) \frac{D_{Veq}}{D_{0,Veq}}^{\mu_{Veq}} exp(-\Lambda_{Veq} D_{Veq}) \tag{4}$$

where $N_{w,Veq}$ is the intercept parameter (in $\mathrm{mm}^{-1}\mathrm{m}^{-3}$), $f(\mu_{Veq})$ and μ_{Veq} parameters are dimensionless, Λ_{Veq} is the slope of the distribution in $1/\mathrm{mm}$ and $D_{0,Veq}$ is the median volume diameter in mm. This Γ-size distribution can be expressed starting from the moments of the snowflakes distributions measured by PIP, as in Bringi and Chandrasekar (2001), taking into account the variable changing from D_{max} to D_{Veq} as follows

$$N_{w,Veq} = N_{w,max} \frac{dD_{max}}{dD_{Veq}} = N_{w,max} \frac{1}{r_s^{1/3}} \tag{5}$$

with

$$D_{0,Veq} = D_{0,max} r_s^{1/3} \tag{6}$$

$$\Lambda_{Veq} = \Lambda_{max} \frac{dD_{max}}{dD_{Veq}} = \Lambda_{max} \frac{1}{r_s^{1/3}} \tag{7}$$

$$\mu_{Veq} = \mu_{max}. \tag{8}$$

In the computations we have used the Γ-modeled size distribution, with the maximum dimension of 2.5 $D_{0,veq}$.

3.3 Multi-frequency Z_e-S relations using DDA scattering model

The DDA model is used to characterize the single scattering properties of snowflakes when described with complex and more realistic shape models. Because of computational reasons, here DDA is not used to compute the scattering properties of the observed snowflakes, but rather the pre-calculated lookup tables (LUT) are utilized for realistically shaped particles. Leinonen and Szyrmer (2015) have published an extensive LUT of backscattering properties for realistically modeled unrimed and rimed snow particles. The shape model is obtained by accurately simulating the microphysical processes that lead to snowflake growth. In particular, the snowflake formation is simulated by aggregation of pristine dendrites and subsequent or simultaneous riming of those aggregates using multiple values of equivalent LWP which in turn determines the degree of riming. The simulation of the riming process provides the scattering database to span through a large range of particle masses and sizes allowing to use those microphysical features to constrain the ice particle scattering properties. Moisseev et al. (2017) have shown that during BAECC experiment snow particles were moderately to heavily rimed, therefore the selection of the database that includes rimed particles appears to be justified. The scattering properties of the simulated particles are in fact picked from the LUT by finding the entries that most closely match the retrieved particle size and mass in von Lerber et al. (2017).

According to the PSD bin sizes of the PIP, the LUT is filtered to find entries which falls within each bin category. Then, using the retrieved $m(D)$ relation determined in von Lerber et al. (2017) the LUT entries are sorted with respect to the difference between their mass, and the expected particle mass is computed using the retrieved $m(D)$ relation. An arbitrary number of 10 entries that most closely match the retrieved $m(D)$ relation are selected and their scattering properties are averaged in order to define the representative backscattering cross section of that particular size range. Larger number of particles can be picked from the LUT in order to represent a larger variability of particle mass, but the effects of including heavier and lighter particles tends to cancel out in the averaging and does not produce notable differences in the final integrated reflectivity value.

It is worth noting that the particles of Leinonen and Szyrmer (2015) are partially horizontally aligned where orientation of their shortest principal axis is, being normally distributed, with the standard deviation of 40 degrees.

4 Results

The results are shown for four snowfall events during BAECC to investigate the consistency of Z_e-S relations at X-, Ka- and W-bands using surface observations. Indeed, ten snowfall cases are available from the BAECC IOP, but only for the selected

four events the millimeter-wave radars (Ka- and W-bands) can be considered well calibrated, in the other cases effects of the radome attenuation cannot be fully compensated. K-means cluster analyses were applied to identify three riming subgroups. The uncertainties of the Z_e-S parametric relations at different frequencies are also investigated using TMM and DDA numerical results. The TMM and DDA results can provide some microphysical insights of the considered snowfall events.

4.1 Analysis of X, Ka and W bands Z_e-S empirical relations

The dataset was divided into three riming classes: light, moderate and heavy rimed (LR, MR and HR) snow, following the same logic used presenting the $m(D)$ relations in von Lerber et al. (2017). They have split cases by using LWP values into three classes, which may be considered to correspond to different degrees of riming. Since, the ice particle mass growth rate due to riming is proportional to LWP along the particle fall trajectory, the LWP can as a proxy for riming (e.g. Moisseev et al., 2017). Given that the growth rate, the riming degree of snowfall may also be influenced by the average particle size, such as D_0. To take all of this into account, the presented four snowfall events were classified into three subgroups using a k-means cluster analysis trained by LWP and D_0. The results are presented in Figure 3 where the three clusters are identified in the LWP-D_0 space. It is worth noting that riming is strongly related to LWP, but almost not dependent on the estimated size D_0 of snow particles. In summary, we have analyzed four events for Ka and W bands, three cases (excepted 20 March 2014) for X band. For the Ka and W band radar observations we have 282 data-samples, that correspond to 1410 measurement minutes, separated into 50.35% of LR, 37.23% of MR and 12.42% of HR. For X band we have 174 data-samples, 870 measurement minutes, divided into 49.42% of LR, 35.06% of MR and 15.52% of HR. In Figures 4, 5 and 6 the derived Z_e-S relations for all radar frequencies and riming classes are presented.

The LR snowfall samples are plotted in Figure 4, showing the retrieved liquid-water-equivalent snowfall rate S from PIP (see in equation (1)) with respect to the measured equivalent reflectivity factor Z_e from the ARM radars. A representation with Z_e in dBZ and S in 10-base logarithm has been chosen to adhere to the log-log model in equation (2). The parameters of the three Z_e-S relations are given in the Table 2. The accuracy of Z_e-S relations has been evaluated using the root mean square error (RMSE) in dB (where the error is defined as the difference between observed Z_e and estimated from PIP LWE, using the regression coefficients). Also the normalized RMSE (NRMSE), RMSE values normalized by the observed reflectivity range, is presented in the table. The NRMSE in percentages of the regressions shown in Figure 4, are about 13% and 10% respectively for X- and Ka-/W-band. Both prefactors and exponents of the Z_e-S relations tend to decrease with the radar frequency increase similar to what is presented in Matrosov (2007) and Matrosov et al. (2008). The regression coefficients are very close to those of Matrosov (2007); Matrosov et al. (2008) and are rather different from those of Boucher and Wieler (1985a) and Fujiyoshi et al. (1990a). The literature values of the Z_e-S relations are summarized in Table 3.

Similar to the light riming class, the MR snowfall Z_e-S observations are shown in Figure 5. The prefactor, a, and exponent, b, are slightly different with respect to the LR snowfall class, they decrease with the frequency but they have lower values, especially for X band. Also the trend of the a-coefficient can be considered in line with Matrosov (2007) and Matrosov et al. (2008), while the b-coefficient is close to Matrosov (2007) and Matrosov et al. (2008) only for W band.

The last result is for HR snowfall, presented in Figure 6. The values of the a- and b-coefficients are lower than those of the previous two riming regimes and than those of Matrosov (2007) and Matrosov et al. (2008), having a worse NRMSE accuracy of about 17% (X band), 14% (Ka band) and 16% (W band).

Using data of the studied snowfall cases, the frequency behavior of the a and b power-law coefficients in Table 2 may be useful to suggest a general trend of the Z_e-S relation, even though only 3 frequency at X, Ka and W band are available. Figure 7 shows the spectral variation of the a and b coefficients, splitting the results between lightly rimed snowfall (black triangles), moderately rimed (black points) and heavily rimed snowfall classes (black squares). The spline interpolation has been introduced for the three riming classes to outline a possible trend for these 2 coefficients. Considering all the limitations of the presented analysis it is still worth noting that: i) the monotonic decrease of the a coefficient with the frequency has been noted for all the three classes in Figure 7 (a); the slope is higher for the LR with respect to the MR and HR. ii) the different spectral trend of the b coefficient in Figure 7 (b) decreases with the frequency but it could be used also to separated the three regimes.

While analyzing the presented Z_e-S relation trends, we should understand that these relations depend on PSD parameters, such as N_w, $m(D)$ and corresponding single-scattering ice particle properties. The difference between Z_e-S obtained for different radar frequency bands, arises from the changes in the snowflake scattering properties. In the Rayleigh regime, the dependence of radar cross section (RCS), on D, is given by $m(D)^2$. For higher frequencies the exponent of $RCS(D)$ relation will become smaller, and therefore the exponent of Z_e-S relation should decrease as well. However, the relations derived for different snowfall riming regimes are influenced not only by changes in $m(D)$, but by changes in PSD. Furthermore, here not only changes in average values of, for example, N_w are important, but also by PSD parameter variations during the recorded events (von Lerber et al., 2017). Therefore, some of the changes in the a and b coefficients between the riming classes is probably caused by the PSD values and variations.

4.2 Explaining Z_e-S relations with scattering simulations

Time-series of multi-frequency radar measurements can provide a further insight into the analysis of snowfall regime and the capability to simulate its behavior. Figure 8 shows the equivalent reflectivity factor Z_e as a function of time for the snow case study of 12 February 2014 predominantly LR case (100% for X band, 91.67% for Ka-/W band). The black triangles and points correspond to ARM-radar mean Z_e, whereas the bars are related to the variation between their minimum and maximum values within the same averaging time interval of 5 minutes. A 8.33% of the measurements (black points in Figure 8(b)-(c)) at the beginning of the event corresponds to the MR snow-data (0% for X band, 8.33% for Ka-/W band) and they are disregarded since the variation index (defined as the ratio between minimum-maximum variability interval and its mean value) is considered to be too high. The different colored lines refer to Z_e, simulated using TMM from PIP data with a variable aspect ratio r_s between 0.2 and 1 with step 0.2. The smaller value r_s=0.2 (red line) indicate very oblate particles, whereas r_s=1.0 (blue line) correspond to spherical snowflakes. By comparing ARM measurements and TMM simulations, the optimal aspect ratio value seems to decrease when increasing the frequency: X-band data are better represented by TMM-derived spherical particles ($r_s = 1$), whereas Ka- and W-band results are in agreement with an aspect ratio of 0.6. After 07:00 UTC within the

heavy precipitation period, no data are available for X-band radar in this case study, but the optimal aspect ratio tend to change to a value around of $r_s = 0.4$ for the millimeter-wave radars (Ka- and W-band). This frequency dependence of the aspect ratio indicates that the soft-spheroid model is not consistent across the frequencies, for this snow event. This finding is in-line with (Leinonen et al., 2012; Kneifel et al., 2015) that showed that for low-density aggregates the soft-spheroid model may not be adequate.

Figure 9 shows again Z_e as a function of time for the 15-16 February 2014, mixed LR/MR snowfall case (61.02% for LR and 38.98% for MR). We can distinguish two main intervals: before the heavy precipitation around 22:10 UTC, as for the previous case, the optimal aspect ratio decreases when increasing the radar frequency, whereas during the heavy precipitation interval (from 22:50 on) the optimal aspect ratio seems to be around 0.6 independently from the frequency that corresponds to the LR time-period. Figure 10 shows the time behavior for the 21-22 February 2014, a snow case with all three regimes present (X band: 13.33% for LR, 56.67% for MR and 30% for HR; Ka/W band: 10.14% for LR, 65.94% for MR and 23.91% for HR). Till 22:00 UTC, in presence of MR snow, the optimal aspect ratios seem to be around 1, 0.8 and 0.8 at X-, Ka- and W-band, respectively, whereas during the heavy precipitation period (23:00-00:00 UTC), in presence of LR snow, it is constant around $r_s = 0.6$ irrespective of the frequency. These considerations are also valid for the 20 March 2014 in Figure 11 in which the optimal aspect ratio is about $r_s = 0.6$ for the millimeter-wave radars (Ka- and W-band) and in fact it was a predominantly LR case (72.41% for LR, 24.14% for MR and 3.45% for HR). For this case X-band data are not available and thus they are not shown in the figure.

As a general comment on Figures 8-11, we note that measured data falls within the computed range of uncertainty. The incremental difference in terms of Z_e due to an increase of 0.2 in the particle aspect ratio is about 1.7 dBZ at X band, 2.5 dBZ at Ka band and 6 dBZ at W band. The difference between the value for $r_s = 0.2$ and $r_s = 1$ is on an average 5.5 dBZ for X-band, 7 dBZ for Ka-band and 12 dBZ for W-band. By increasing the frequency from X- to W-band, the radar reflectivity seems to be, in general, more sensitive to the non-spherical shape of the snowflakes with r_s going from 1 down to 0.6.

To investigate how the soft-spheroid model performs in terms of reproducing the observed Z_e-S relations, the TMM computed reflectivity factors were used to derive multi-frequency Z_e-S relations. The relations were computed using different values of the soft-spheroid model aspect ratio. The derived relations are summarized in Table 2 and shown in Fig. 4, 5, and 6. Similar to the analysis of the Z_e time-series, presented above, we may conclude that to reproduce the observed Z_e-S relations at different frequencies different spheroid aspect ratios may need to be used. This effect is clearest for the LR class, see Fig. 4, where for X-band the best fitting aspect ratio is 1 and for W-band it is closer to 0.6. For heavier rimed particles this difference becomes less pronounced.

It should be noted that the observed differences between observed Z_e and ones computed using TMM are not as large as was previously expected. To investigate why this is the case, single-scattering properties computed using DDA (Leinonen and Szyrmer, 2015) were compared to the TMM results for the three cases shown in Fig. 12. The computations are performed for the W-band. TMM simulations are given by red, green and blue lines referring to different aspect ratios ($r_s = 0.2,\ 0.6,\ 1$, respectively), whereas DDA results are given by the black line. The dotted line shows the product between the snowflake PSD and the RCS computed using TMM with aspect ratio of 0.6 (green dotted line) and the DDA (black dotted line). This

figure shows that TMM computations using lower aspect ratios agree better with DDA. Furthermore, it indicates that there is a compensating effect, where TMM overestimates RCS for smaller snowflakes and underestimates it for larger particles. This may explain smaller differences between the DDA and TMM calculations.

This compensation effect depends on the integration limits used to compute the Z_e. In this study we have integrated from 0 to 2.5 D_0. To check whether this integration limit is valid, in Fig. 13 measured and fitted PSD are shown. As can be seen the assumed upper integration limit appears to be valid..

5 Conclusions

The multi-frequency Z_e-S relationships at X-, Ka- and W-bands have been investigated in this work using a dataset of zenith-pointing radar data and in-situ measurements acquired during the BAECC campaign.

From a data analysis point of view, adopting as a reference a power-law relation, regression coefficients have been extracted for characterizing Z_e-S at the considered frequency bands. These coefficients are in line with those provided in literature and confirm also the applicability of a power-law empirical model to the millimeter-wave radars for snowfall estimation in different riming regimes. The latter can be schematically refer to as light, moderate and heavy rimed snowfall.

For validation and intercomparison, numerical simulations have been also carried out using the soft-spheroid model and TMM, coupled with microphysical sizing from an in-situ video-disdrometer and a new mass-dimensional relation and using the particle aspect-ratio as a tuning parameter. Uncertainty of each derived relationship has been provided and ranked with respect to the available radar measurements of BAECC IOP . The latter show that there are specific spheroid aspect ratios for the three identified snowfall regimes. TMM numerical results have been also compared with DDA scattering simulation in order to better understand the role of the aspect-ratio.

Uncertainty evaluation has been attached to each empirical and modeled power-law relationship at X, Ka and W band for each case study and for the three snowfall regimes. This set of regression coefficients may be used in the future for selecting optimal Z_e-S algorithms in different geographical regions and to assess the dependence on the snowfall type. In this respect, the results of this work can represent a first step towards the design of snowfall retrieval algorithm derived from ground-based measurements and the set-up of simplified scattering simulations for radar centimeter and millimeter wavelength.

Acknowledgements. MTF has been partly supported by the Center of Excellence CETEMPS, L'Aquila (Italy). The activity of the author DO was funded by the German Research Foundation (DFG) as part of the Emmy-Noether Group OPTIMIce under grant KN 1112/2-1. The author AvL was supported by Horizon 2020 grant agreements No 699221 (PNOWWA) and No 700099 (ANYWHERE). The research of DM was supported by Academy of Finland (grant 305175) and the Academy of Finland Finnish Center of Excellence program (grant 3073314). DM also acknowledges the funding received by ERA-PLANET, trans-national project iCUPE (Grant Agreement n. 689443), funded under the EU Horizon 2020 Framework Programme.

References

Böhm, H.: A General Equation for the Terminal Fall Speed of Solid Hydrometeors, Journal of Atmospheric Sciences, 46, 2419 – 2427, doi:10.1175/1520-0469(1989)046<2419:AGEFTT>2.0.CO;2, 1989.

Botta, G., Aydin, K., and Verlinde, J.: Modeling of Microwave Scattering From Cloud Ice Crystal Aggregates and Melting Aggregates: A New Approach., IEEE Geoscience and Remote Sensing Letters, 7, 572–576, doi:10.1109/LGRS.2010.2041633, 2010.

Boucher, R. J. and Wieler, J.: Radar determination of snowfall rate and accumulation., 24, 68–73, 1985a.

Boucher, R. J. and Wieler, J. G.: Radar determination of snowfall rate and accumulation., Journal of climate and applied meteorology, 24, 68–73, doi:10.1175/1520-0450(1985)024<0068:RDOSRA>2.0.CO;2, http://dx.doi.org/10.1175/1520-0450(1985)024<0068:RDOSRA>2.0.CO;2, 1985b.

Bringi, V. and Chandrasekar, V.: Polarimetric Doppler Weather Radar: Principles and Applications., Cambridge University Press, doi:doi:10.1017/CBO9780511541094, 2001.

Cadeddu, M.: Microwave radiometer (MWRLOS), ARM Mobile Facility TMP, University of Helsinki research station SMEAR II, Hyytiälä, Finland. Atmospheric Radiation Measurement (ARM) Climate Research Facility Data Archive, Oak Ridge, TN, accessed 17 March 2016., 2014.

Carlson, P. E. and Marshall, J. S.: Measurement of Snowfall by Radar., Journal of Applied Meteorology, 11, 494–500, doi:10.1175/1520-0450(1972)011<0494:MOSBR>2.0.CO;2, http://dx.doi.org/10.1175/1520-0450(1972)011<0494:MOSBR>2.0.CO;2, 1972.

Dungey, C. and Bohren, C.: Backscattering by Nonspherical Hydrometeors as Calculated by the Coupled-Dipole Method: An Application in Radar Meteorology., Journal of Atmospheric and Oceanic Technology, 10, 526–532, doi:http://dx.doi.org/10.1175/1520-0426(1993)010<0526:BBNHAC>2.0.CO;2, 1993.

Fujiyoshi, Y., Endoh, T., T., Y., Tsuboki, K., Tachibana, Y., and Wakahama, G.: Determination of a Z-R Relationship for Snowfall Using a Radar and High Sensitivity Snow Gauges., Journal of Applied Meteorology, 29, 147–152, doi:10.1175/1520-0450(1990)029<0147:DOARFS>2.0.CO;2, http://dx.doi.org/10.1175/1520-0450(1990)029<0147:DOARFS>2.0.CO;2, 1990a.

Fujiyoshi, Y., Endoh, T., Yamada, T., Tsuboki, K., Tachibana, Y., and Wakahama, G.: Determination of a Z-R relationship for snowfall using a radar and high sensitivity snow gauges., 29, 147–152, 1990b.

Goodison, B., Louie, P., and Yang, D.: WMO solid precipitation measurement intercomparison final report, Tech. Rep. WMO/TD No.872, IOM No. 67, 1998.

Gorgucci, E., Scarchilli, G., and Chandrasekar, V.: Calibration of radars using polarimetric techniques, 30, 853 – 858, 1992.

Gourley, J., Illingworth, A., and Tabary, P.: Absolute Calibration of Radar Reflectivity Using Redundancy of the Polarization Observations and Implied Constraints on Drop Shapes., 26, 689 – 703, 2009.

Gunn, K. L. S. and Marshall, J. S.: The distribution with size of aggregate snowflakes., Journal of Meteorology, 15, 452–461, doi:10.1175/1520-0469(1958)015<0452:TDWSOA>2.0.CO;2, http://dx.doi.org/10.1175/1520-0469(1958)015<0452:TDWSOA>2.0.CO;2, 1958.

Hogan, R. J., Illingworth, A. J., and Sauvageot, H.: Measuring Crystal Size in Cirrus Using 35- and 94-GHz Radars., Journal of Atmospheric and Oceanic Technology, 17, 27–37, doi:10.1175/1520-0426(2000)017<0027:MCSICU>2.0.CO;2, http://dx.doi.org/10.1175/1520-0426(2000)017<0027:MCSICU>2.0.CO;2, 2000.

Huuskonen, A. and Holleman, I.: Determining Weather Radar Antenna Pointing Using Signals Detected from the Sun at Low Antenna Elevations., Journal of Atmospheric and Oceanic Technology, 24, 476–483, doi:10.1175/JTECH1978.1, http://dx.doi.org/10.1175/JTECH1978.1, 2010.

Illingworth, A. J., Hogan, R. J., O'Connor, E. J., Bouniol, D., Delanoë, J., Pelon, J., Protat, A., Brooks, M. E., Gaussiat, N., Wilson, D. R., Donovan, D. P., Baltink, H. K., van Zadelhoff, G.-J., Eastment, J. D., Goddard, J. W. F., Wrench, C. L., Haeffelin, M., Krasnov, O. A., Russchenberg, H. W. J., Piriou, J.-M., Vinit, F., Seifert, A., Tompkins, A. M., and Willén, U.: Cloudnet, Bulletin of the American Meteorological Society, 88, 883–898, doi:10.1175/BAMS-88-6-883, 2007.

Illingworth, A. J., Barker, H. W., Beljaars, A., Ceccaldi, M., Chepfer, H., Clerbaux, N., Cole, J., Delanoë, J., Domenech, C., Donovan, D. P., Fukuda, S., Hirakata, M., Hogan, R. J., Huenerbein, A., Kollias, P., Kubota, T., Nakajima, T., Nakajima, T. Y., Nishizawa, T., Ohno, Y., Okamoto, H., Oki, R., Sato, K., Satoh, M., Shephard, M. W., Velázquez-Blázquez, A., Wandinger, U., Wehr, T., and van Zadelhoff, G.-J.: The EarthCARE Satellite: The Next Step Forward in Global Measurements of Clouds, Aerosols, Precipitation, and Radiation, Bulletin of the American Meteorological Society, 96, 1311–1332, doi:10.1175/BAMS-D-12-00227.1, https://doi.org/10.1175/BAMS-D-12-00227.1, 2015.

Kneifel, S., Kulie, M. S., and Bennartz, R.: A triple-frequency approach to retrieve microphysical snowfall parameters, Journal of Geophysical Research: Atmospheres, 116, n/a–n/a, doi:10.1029/2010JD015430, http://dx.doi.org/10.1029/2010JD015430, d11203, 2011.

Kneifel, S., von Lerber, A., Tiira, J., Moisseev, D., Kollias, P., and Leinonen, J.: Observed relations between snowfall microphysics and triple-frequency radar measurements., Journal of Geophysical Research: Atmospheres, 120, 6034–6055, doi:10.1002/2015JD023156, http://dx.doi.org/10.1002/2015JD023156, 2015.

Kneifel, S., Neto, J. D., Ori, D., Moisseev, D., Tyynela, J., Adams, I., Kuo, K., Bennartz, R., Berne, B., Clothiaux, E., Eriksson, P., Geer, A. J., Honeyager, R., Leinonen, J., and Westbrook, C.: The First International Summer Snowfall Workshop: Scattering properties of realistic frozen hydrometeors from simulations and observations, as well as defining a new standard for scattering databases, Bulletin of the American Meteorological Society, 0, null, doi:10.1175/BAMS-D-17-0208.1, 2018.

Kollias, P., Miller, M. A., Luke, E. P., Johnson, K. L., Clothiaux, E. E., Moran, K. P., Widener, K. B., and Albrecht, B. A.: The Atmospheric Radiation Measurement Program Cloud Profiling Radars: Second-Generation Sampling Strategies, Processing, and Cloud Data Products., Journal of Atmospheric and Oceanic Technology, 24, 1199–1214, doi:10.1175/JTECH2033.1, http://dx.doi.org/10.1175/JTECH2033.1, 2007.

Kulie, M. S., Hiley, M. J., Bennartz, R., Kneifel, S., and Tanelli, S.: Triple-Frequency Radar Reflectivity Signatures of Snow: Observations and Comparisons with Theoretical Ice Particle Scattering Models, Journal of Applied Meteorology and Climatology, 53, 1080–1098, doi:10.1175/JAMC-D-13-066.1, 2014.

Leinonen, J.: High-level interface to T-matrix scattering calculations: architecture, capabilities and limitations, Opt. Express, 22, 1655–1660, doi:10.1364/OE.22.001655, http://www.opticsexpress.org/abstract.cfm?URI=oe-22-2-1655, 2014.

Leinonen, J. and Szyrmer, W.: Radar signatures of snowflake riming: A modeling study, Earth and Space Science, 2, 346–358, doi:10.1002/2015EA000102, http://dx.doi.org/10.1002/2015EA000102, 2015EA000102, 2015.

Leinonen, J., Kneifel, S., Moisseev, D., Tyynelä, J., Tanelli, S., and Nousiainen, T.: Evidence of nonspheroidal behavior in millimeter-wavelength radar observations of snowfall, Journal of Geophysical Research: Atmospheres, 117, n/a–n/a, doi:10.1029/2012JD017680, http://dx.doi.org/10.1029/2012JD017680, d18205, 2012.

Liebe, H. J.: An updated model for millimeter wave propagation in moist air., Radio Science, 20, 1069–1089, doi:10.1029/RS020i005p01069, http://dx.doi.org/10.1029/RS020i005p01069, 1985.

Magono, C. and Nakamura, T.: Aerodynamic studies of falling snowflakes., Journal of the Meteorological Society of Japan. Ser. II, 43, 139–147, doi:10.2151/jmsj1965.43.3_139, 1965.

Matrosov, S. Y.: Radar reflectivity in snowfall., IEEE Transactions on Geoscience and Remote Sensing, 30, 454–461, doi:10.1109/36.142923, http://ieeexplore.ieee.org/stamp/stamp.jsptp=&arnumber=142923&isnumber=3834, 1992.

Matrosov, S. Y.: Modeling Backscatter Properties of Snowfall at Millimeter Wavelengths., Journal of the Atmospheric Sciences, 64, 1727–1736, doi:10.1175/JAS3904.1, http://dx.doi.org/10.1175/JAS3904.1, 2007.

Matrosov, S. Y., D., S. M., and Djalalova, I. V.: Snowfall Retrievals Using Millimeter-Wavelength Cloud Radars., Journal of Applied Meteorology and Climatology, 47, 769–777, doi:10.1175/2007JAMC1768.1, http://dx.doi.org/10.1175/2007JAMC1768.1, 2008.

Matrosov, S. Y., Campbell, C., Kingsmill, D., and Sukovich, E.: Assessing snowfall rates from X-band radar reflectivity measurements., Journal of Atmospheric and Oceanic Technology, 26, 2324–2339, 2009.

Mishchenko, M. I.: Calculation of the amplitude matrix for a nonspherical particle in a fixed orientation., Applied Optics, 39, 1026–1031, doi:10.1364/AO.39.001026, http://ao.osa.org/abstract.cfm?URI=ao-39-6-1026, 2000.

Mitchell, D. L.: Evolution of snow-size spectra in cyclonic storms. Part I: Snow growth by vapor deposition and aggregation., Journal of the atmospheric sciences, 45, 3431–3451, doi:10.1175/1520-0469(1988)045<3431:EOSSSI>2.0.CO;2, http://dx.doi.org/10.1175/1520-0469(1988)045<3431:EOSSSI>2.0.CO;2, 1988.

Mitchell, D. L. and Heymsfield, A. J.: Refinements in the Treatment of Ice Particle Terminal Velocities, Highlighting Aggregates, Journal of Atmospheric Sciences, 62, 1637 – 1644, doi:10.1175/JAS3413.1, 2005.

Moisseev, D., von Lerber, A., and Tiira, J.: Quantifying the effect of riming on snowfall using ground-based observations, Journal of Geophysical Research: Atmospheres, 122, 4019–4037, doi:10.1002/2016JD026272, http://dx.doi.org/10.1002/2016JD026272, 2016JD026272, 2017.

Newman, A. J., Kucera, P. A., and Bliven, L. F.: Presenting the Snowflake Video Imager (SVI)., Journal of Atmospheric and Oceanic Technology, 26, 167–179, doi:10.1175/2008JTECHA1148.1, http://dx.doi.org/10.1175/2008JTECHA1148.1, 2009.

Nešpor, V., Krajewski, W. F., and A., K.: Wind-Induced Error of Raindrop Size Distribution Measurement Using a Two-Dimensional Video Disdrometer., Journal of Atmospheric and Oceanic Technology, 17, 1483–1492, doi:10.1175/1520-0426(2000)017<1483:WIEORS>2.0.CO;2, http://dx.doi.org/10.1175/1520-0426(2000)017<1483:WIEORS>2.0.CO;2, 2000.

Petaja, T., O'Connor, E. J., Moisseev, D., Sinclair, V. A., Manninen, A. J.and Väänänen, R., von Lerber, A., Thornton, J. A., Nicoll, K., Petersen, W., Chandrasekar, V., Smith, J. N., Winkler, P. M., Krüger, O., Hakola, H., Timonen, H., Brus, D., Laurila, T., Asmi, E., Riekkola, M.-L., Mona, L., Massoli, P., Engelmann, R., Komppula, M., Wang, J., Kuang, C., Bäck, J., Virtanen, A., Levula, J., Ritsche, M., and Hickmon, N.: BAECC: A Field Campaign to Elucidate the Impact of Biogenic Aerosols on Clouds and Climate., Bulletin of the American Meteorological Society, 97, 1909–1928, doi:10.1175/BAMS-D-14-00199.1, http://dx.doi.org/10.1175/BAMS-D-14-00199.1, 2016.

Petty, G. W. and Huang, W.: Microwave Backscatter and Extinction by Soft Ice Spheres and Complex Snow Aggregates., Journal of the Atmospheric Sciences, 67, 769–787, doi:10.1175/2009JAS3146.1, http://dx.doi.org/10.1175/2009JAS3146.1, 2010.

Rasmussen, R., Dixon, M., Vasiloff, S., Hage, F., Knight, S., Vivekanandan, J., and Xu, M.: Snow Nowcasting Using a Real-Time Correlation of Radar Reflectivity with Snow Gauge Accumulation., Journal of Applied Meteorology, 42, 20–36, doi:10.1175/1520-0450(2003)042<0020:SNUART>2.0.CO;2, http://dx.doi.org/10.1175/1520-0450(2003)042<0020:SNUART>2.0.CO;2, 2003.

Saltikoff, E., Huuskonen, A., Hohti, H., Koistinen, J., and Jarvinen, H.: Quality assurance in the FMI Doppler weather radar network., Boreal environment research, 15, 579–594, 2010.

Sekelsky, S. M.: Near-Field Reflectivity and Antenna Boresight Gain Corrections for Millimeter-Wave Atmospheric Radars., Journal of Atmospheric and Oceanic Technology, 19, 468–477, doi:10.1175/1520-0426(2002)019<0468:NFRAAB>2.0.CO;2, http://dx.doi.org/10.1175/1520-0426(2002)019<0468:NFRAAB>2.0.CO;2, 2002.

Sekhon, R. S. and Srivastava, R. C.: Snow size spectra and radar reflectivity., Journal of the Atmospheric Sciences, 27, 299–307, doi:10.1175/1520-0469(1970)027<0299:SSSARR>2.0.CO;2, http://dx.doi.org/10.1175/1520-0469(1970)027<0299:SSSARR>2.0.CO;2, 1970.

Sihvola, A.: Electromagnetic Mixing Formulas and Applications, The Institution of Electrical Engineers, London, 1999.

Skofronick-Jackson, G., Petersen, W. A., Berg, W., Kidd, C., Stocker, E. F., Kirschbaum, D. B., Kakar, R., Braun, S. A., Huffman, G. J., Iguchi, T., Kirstetter, P. E., Kummerow, C., Meneghini, R., Oki, R., Olson, W. S., Takayabu, Y. N., Furukawa, K., and Wilheit, T.: The Global Precipitation Measurement (GPM) Mission for Science and Society, Bulletin of the American Meteorological Society, 98, 1679–1695, doi:10.1175/BAMS-D-15-00306.1, https://doi.org/10.1175/BAMS-D-15-00306.1, 2017.

Stephens, G. L., Vane, D. G., Boain, R. J., Mace, G. G., Sassen, K., Wang, Z., Illingworth, A. J., O'Connor, E. J., Rossow, W. B., Durden, S. L., Miller, S. D., Austin, R. T., Benedetti, A., Mitrescu, C., and Team, T. C. S.: THE CLOUDSAT MISSION AND THE A-TRAIN, Bulletin of the American Meteorological Society, 83, 1771–1790, doi:10.1175/BAMS-83-12-1771, https://doi.org/10.1175/BAMS-83-12-1771, 2002.

Tiira, J., Moisseev, D. N., von Lerber, A., Ori, D., Tokay, A., Bliven, L. F., and Petersen, W.: Ensemble mean density and its connection to other microphysical properties of falling snow as observed in Southern Finland., Atmospheric Measurement Techniques, 9, 4825–4841, doi:10.5194/amt-9-4825-2016, http://www.atmos-meas-tech.net/9/4825/2016/, 2016.

Tyynelä, J., Leinonen, J., Moisseev, D., and Nousiainen, T.: Radar Backscattering from Snowflakes: Comparison of Fractal, Aggregate, and Soft Spheroid Models., Journal of Atmospheric and Oceanic Technology, 28, 1365–1372, doi:10.1175/JTECH-D-11-00004.1, http://dx.doi.org/10.1175/JTECH-D-11-00004.1, 2011.

von Lerber, A., Moisseev, D., Bliven, L. F., Petersen, W., Harri, A., and Chandrasekar, V.: Microphysical Properties of Snow and Their Link to Ze-S Relations during BAECC 2014, Journal of Applied Meteorology and Climatology, 56, 1561–1582, doi:10.1175/JAMC-D-16-0379.1, 2017.

Table 1. Radar technical specifications are shown for C-band polarimetric Doppler weather radar and for the ARM cloud radar systems at X-, Ka- and W-band.

Acronym	IKA	XSACR	KAZR	MWACR
Location	Ikaalinen	Hyytiälä	Hyytiälä	Hyytiälä
Frequency (GHz)	5.6	9.7	35.3	95.0
Beam width (°)	0.94–0.98	1.27	0.33	0.38
Sensitivity at 1 km (dBZ)	-48	-30[a]	-50[a]	-50[a]
Range gate spacing (m)	-	25	25	30
Temporal sampling	15 min	2 s	2 s	2 s

[a] Sensitivity for 2 s integration time and for nominal ARM radar settings.

Table 2. Empirical Z_e-S for the four snow cases divided to LR, MR and HR snowfall regimes as shown in Fig. 4-6. Z_e-S at X-, Ka- and W-band derived from ARM radar and PIP video-disdrometer using a least-square regressive analysis in the log-log space for each riming regime. The root-mean-square error (RMSE) is also shown as well as the Normalized RMSE (NRMSE) using for normalization the value range (defined as the maximum value minus the minimum value) of the measured data as normalization. The variability of coefficients, a and b, has been shown in Figure 7. Coefficients are related to the Z_e-S reference model in power-law form that is $Z_e = aS^b$ where Z_e is expressed in $\mathrm{mm^6 m^{-3}}$ and S is in $\mathrm{mm/h}$.

Regime	Band	a	b	RMSE dB	NRMSE adim.
LR	X	60.98	1.29	4.68	0.13
LR	Ka	38.42	1.10	3.32	0.10
LR	W	9.09	0.97	3.19	0.10
MR	X	41.80	0.96	4.11	0.12
MR	Ka	33.28	0.88	3.85	0.11
MR	W	7.45	0.79	3.34	0.11
HR	X	48.34	0.80	4.42	0.17
HR	Ka	32.62	0.75	3.30	0.14
HR	W	7.76	0.73	3.33	0.16

BAECC cases of snowfall events with the a-b coefficients estimated in a 5-minute time window.

Table 3. The prefactors and exponents of the Z_e-S relation in the literature for X-, Ka- and W-band.

Literature	Band	a	b
Boucher and Wieler (1985a)[1]	X	150 (220)	1.65 (1.65)
Fujiyoshi et al. (1990b)[2]	X	427,554	1.09, 0.88
Matrosov et al. (2009)	X	30-140	1.3-1.55
Matrosov (2007)-Matrosov et al. (2008)	Ka	56	1.20
Matrosov (2007)-Matrosov et al. (2008)	W	10	0.8

[1] Boucher and Wieler (1985a) provided a mean X-band relation between snowfall depth S_S and equivalent radar reflectivity as $Z_e = 5.07 S_S^{1.65}$. This relation is expressed in Table for the snow-to-liquid ratio of $8:1$ $(10:1)$.

[2] Fujiyoshi et al. (1990b) presented a best-fit power-law relationship using 1-minute and 30-minute respectively of averaged S and Z_e.

Table 4. For all three riming classes Z_e-S (with Z_e in $\mathrm{mm^6 m^{-3}}$, S in $\mathrm{mmh^{-1}}$) relationships, derived from TMM-based numerical simulations of Z_e and PIP-derived S and using the oblate-particle aspect ratio as a tuning parameter between 0.2 and 1. The best Z_e-S relation is highlighted in bold and corresponds to the power-law minimizing both RMSE and NRMSE.

Regime	Band	Z_e-S (r_s=0.2)	RMSE dBZ	NRMSE adim.	Z_e-S (r_s=0.4)	RMSE dBZ	NRMSE adim.	Z_e-S (r_s=0.6)	RMSE dBZ	NRMSE adim.	Z_e-S (r_s=0.8)	RMSE dBZ	NRMSE adim.	Z_e-S (r_s=1)	RMSE dBZ	NRMSE adim.
LR	X	$171.52S^{1.36}$	6.26	0.17	$96.92S^{1.39}$	4.94	0.13	$\mathbf{69.52S^{1.39}}$	**4.71**	**0.13**	$54.11S^{1.38}$	4.81	0.13	$43.81S^{1.38}$	5.06	0.14
	Ka	$124.72S^{1.24}$	5.67	0.16	$59.64S^{1.23}$	3.67	0.11	$\mathbf{36.36S^{1.20}}$	**3.43**	**0.10**	$23.77S^{1.16}$	4.08	0.12	$16.09S^{1.13}$	5.11	0.15
	W	$78.61S^{1.12}$	9.36	0.30	$23.96S^{1.05}$	5.04	0.16	$\mathbf{9.59S^{0.98}}$	**3.20**	**0.10**	$4.31S^{0.93}$	4.43	0.14	$2.10S^{0.90}$	6.86	0.22
MR	X	$153.10S^{1.13}$	6.50	0.20	$106.69S^{1.13}$	5.41	0.16	$76.87S^{1.11}$	4.67	0.14	$61.63S^{1.10}$	4.33	0.13	$\mathbf{51.64S^{1.08}}$	**4.19**	**0.13**
	Ka	$162.22S^{1.12}$	6.94	0.20	$90.90S^{1.07}$	5.22	0.15	$54.85S^{1.03}$	4.19	0.12	$\mathbf{36.24S^{0.98}}$	**3.90**	**0.11**	$24.86S^{0.94}$	4.19	0.12
	W	$93.78S^{1.00}$	10.49	0.36	$36.11S^{0.92}$	7.06	0.24	$14.14S^{0.85}$	4.17	0.14	$\mathbf{6.32S^{0.80}}$	**3.42**	**0.12**	$3.08S^{0.76}$	4.96	0.17
HR	X	$31.90S^{0.67}$	4.55	0.18	$56.42S^{0.76}$	4.52	0.18	$\mathbf{58.04S^{0.85}}$	**4.45**	**0.18**	$56.96S^{0.91}$	4.46	0.18	$54.46S^{0.95}$	4.52	0.18
	Ka	$25.24S^{0.56}$	3.47	0.14	$42.34S^{0.67}$	3.79	0.16	$\mathbf{36.50S^{0.75}}$	**3.33**	**0.14**	$30S^{0.81}$	3.41	0.14	$23.98S^{0.85}$	3.95	0.16
	W	$11.65S^{0.54}$	4.77	0.23	$\mathbf{13.45S^{0.62}}$	**4.70**	**0.23**	$10S^{0.76}$	3.43	0.17	$6.68S^{0.87}$	3.88	0.19	$4.33S^{0.95}$	5.59	0.27

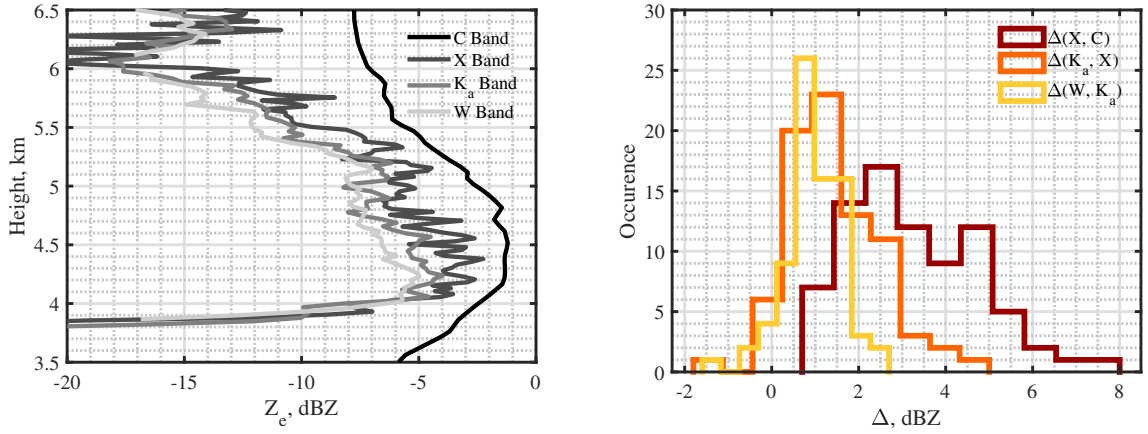

Figure 1. Left panel (a) shows radar profiles at C-, X-, Ka- and W-band for the 15 February 2014 at 17:13 UTC where calibration is performed within in the most stable height interval between 4 and 6 km. Right panel (b) shows calibration error histograms related to the differences (Δ) between X- and C- band radars (dark red), Ka- and X-band radars (orange), and W- and Ka-radars (yellow).

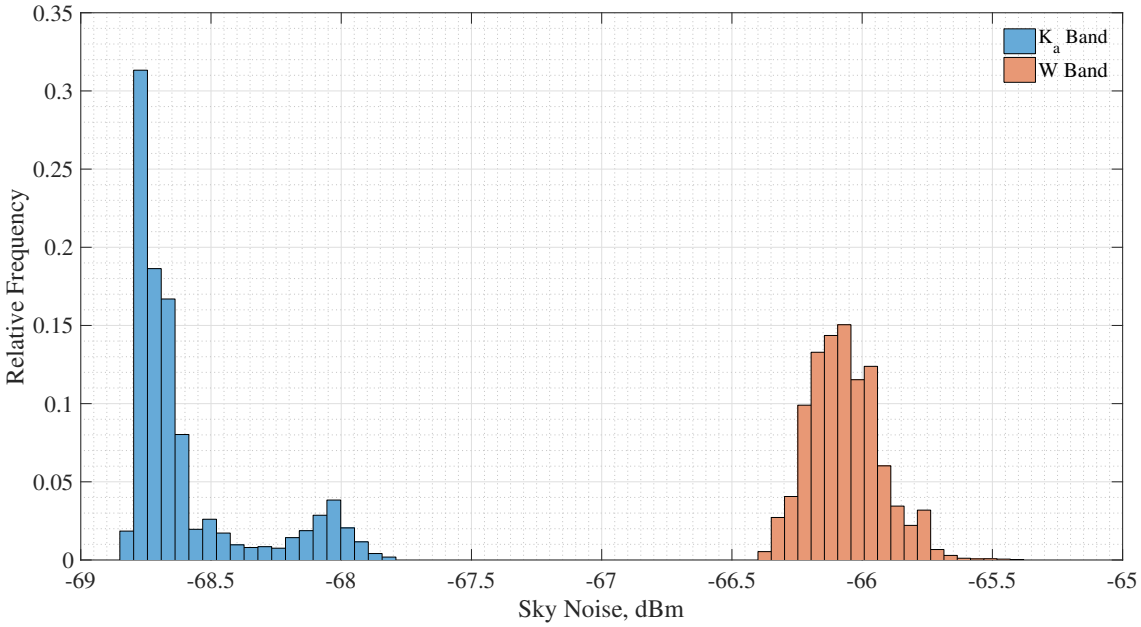

Figure 2. Relative frequency histograms of the sky noise antenna temperature for the Ka- and W-band radars for all 10 days of BAECC IOP campaign.

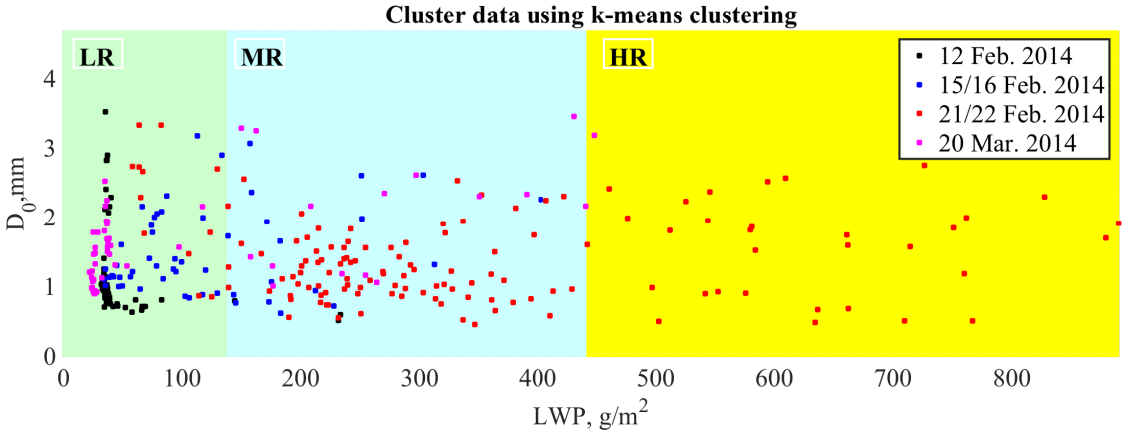

Figure 3. Plot of median diameter D_0 with respect to LWP for the three cluster regions, LR, MR and HR, (green, cyan, yellow) obtained on four snowfall days of BAECC IOP campaign. The black, blue, red and magenta points represent respectively the data for 12, 15/16, 21/22 February and 20 March 2014. The k-means clustering highlights the weak dependence of the classes from D_0.

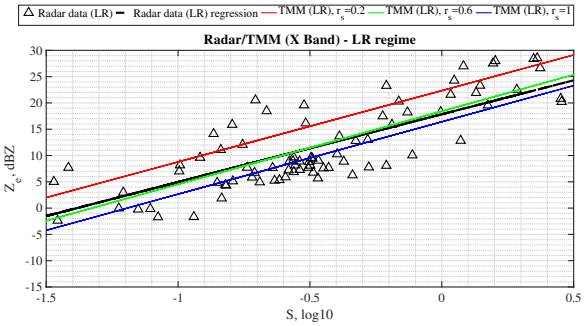

(a)

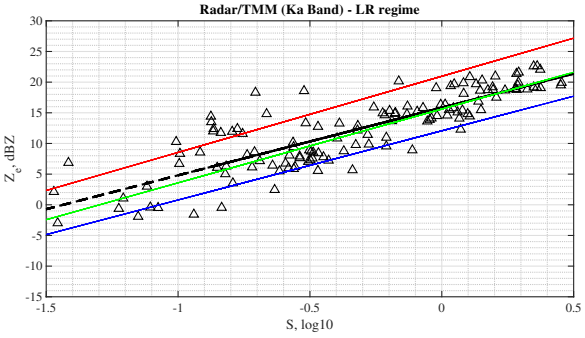

(b)

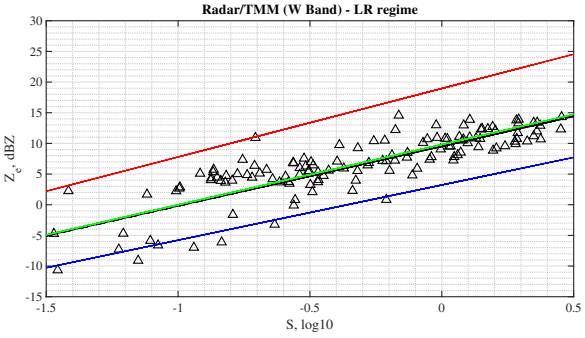

(c)

Figure 4. Case for light rimed (LR) snowfall, starting from the top: X-, Ka- and W-band result. Scatter plot of the equivalent radar reflectivity, measured by ARM radars (black triangles), with respect to the snow rates S, measured by PIP. The black line represents the Z_e-S empirical least-square relationship as listed in Table 2. Z_e-S parametric relations, derived from TMM-based simulations, are also shown for different aspect ratios (0.2, 0.6, 1) using red, green and blue lines as listed in Table 4.

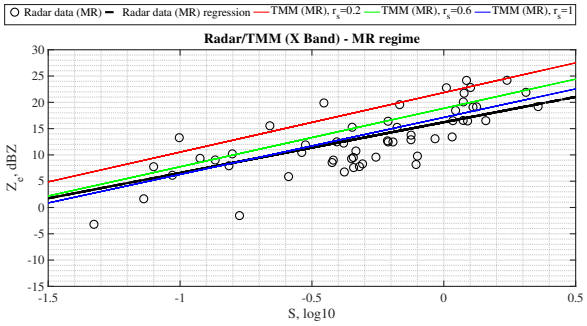

(a)

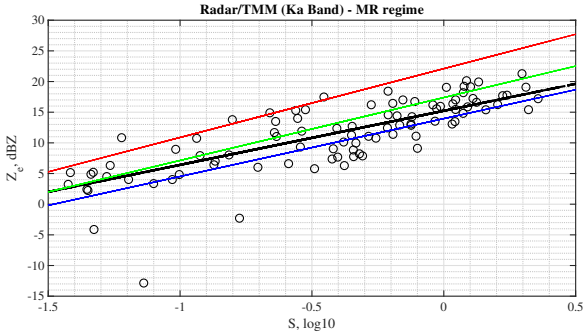

(b)

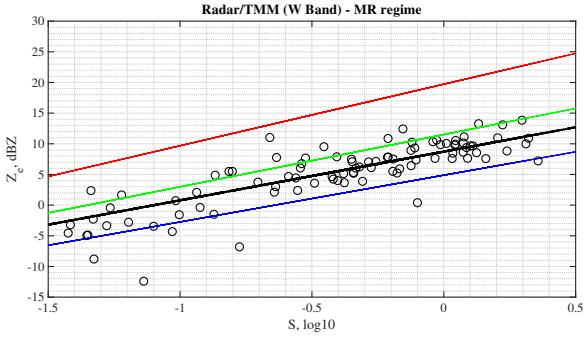

(c)

Figure 5. Same as Figure 4, but for moderate rimed (MR) snowfall case. Scatterplot is now represented by black points.

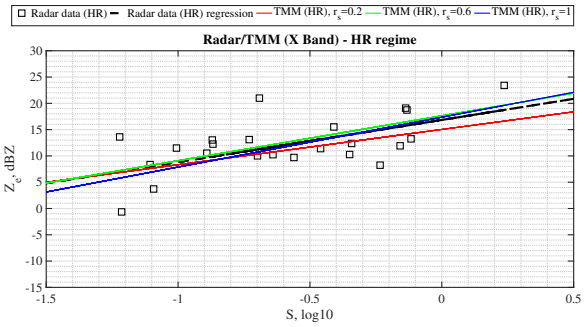

(a)

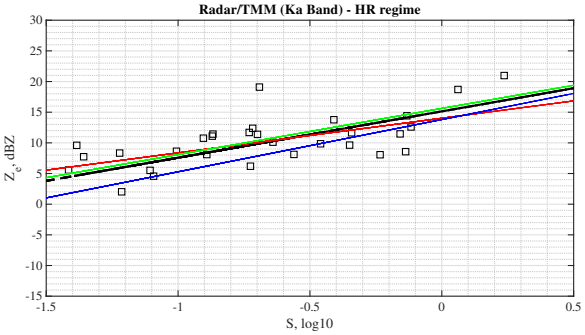

(b)

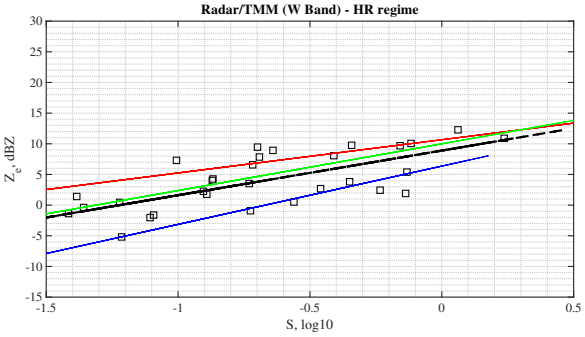

(c)

Figure 6. Same as Figure 4, but for heavy rimed (HR) snowfall case. Scatterplot is now represented by black squares.

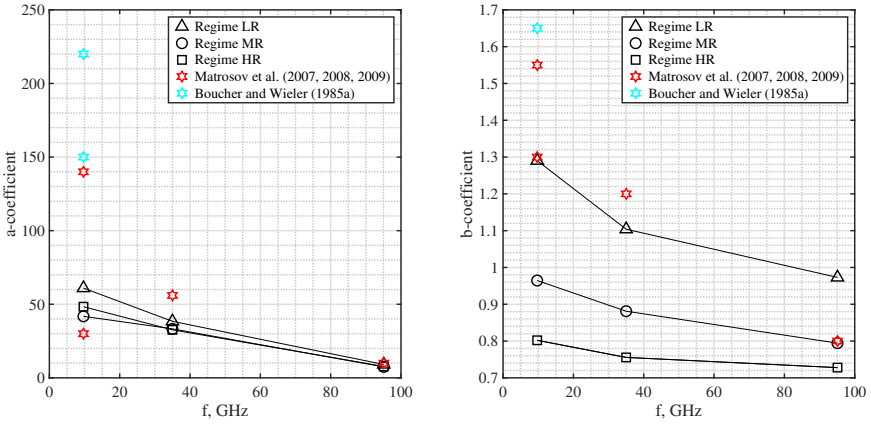

(a) a-coefficient

(b) b-coefficient

Figure 7. Frequency trend for the a (left panel) and b (right panel) regression coefficients, estimated in Table 2 using the power-law form $Z_e = aS^b$ for the four studied snowfall cases divided to LR, MR and HR.

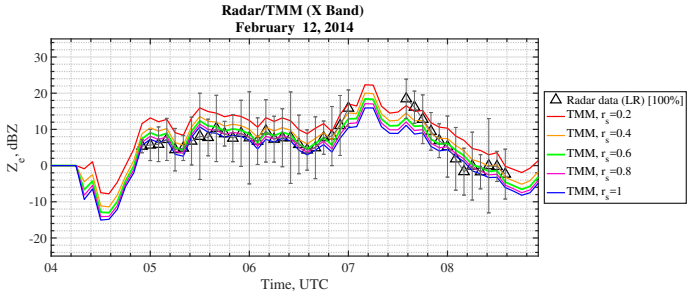

(a)

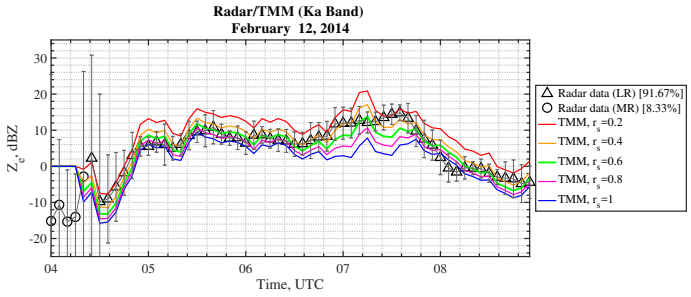

(b)

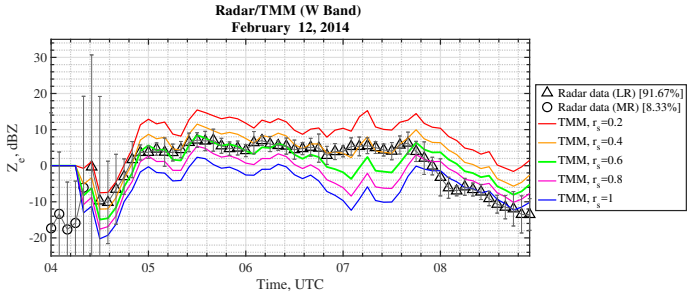

(c)

Figure 8. Radar and TMM computations from 12 February 2014 between 04:00 and 08:50 UTC. Radar reflectivities (LR and MR snowfall in black triangles and points respectively) from XSACR, KAZR and MWACR are corrected for sky-noise, calibration offsets and attenuations (as better explained in Section 2.4). The error bars are used to represent the variation (min-max difference) of radar data within a 5-minute window with respect to their averaged value (black triangles and points). TMM-based computations (red, orange, green, magenta, blue lines for $r_s = 0.2$, $r_s = 0.4$, $r_s = 0.6$,$r_s = 0.8$ and $r_s = 1$, respectively) are derived from PIP data.

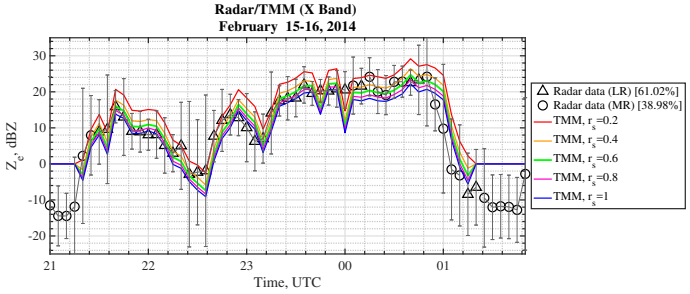

(a)

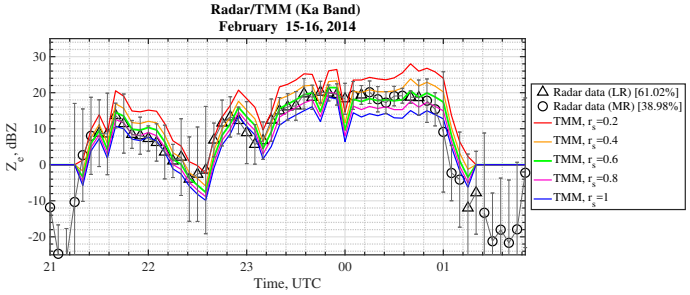

(b)

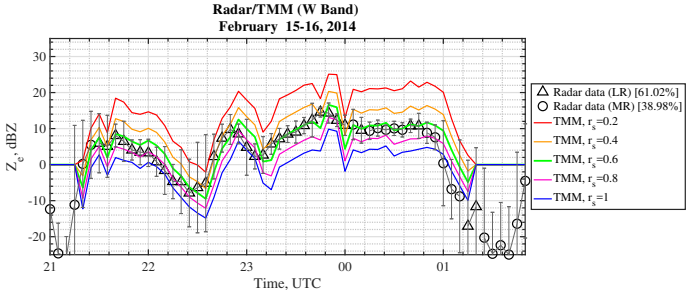

(c)

Figure 9. Same as Figure 8, but for 15/16 February 2014, 21:00-01:48 UTC (LR and MR snowfall in black triangles and points respectively).

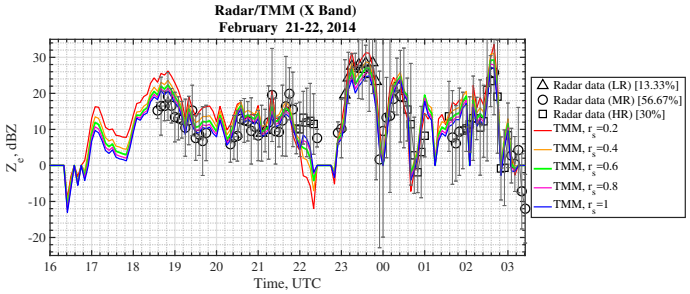

(a)

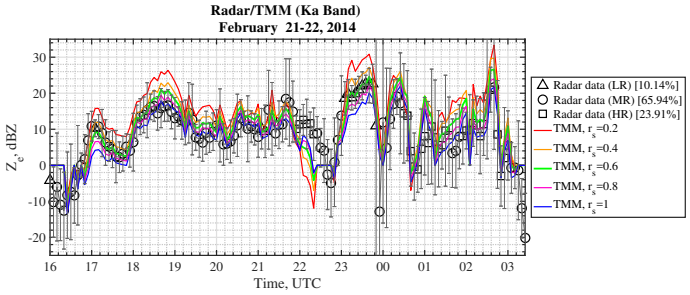

(b)

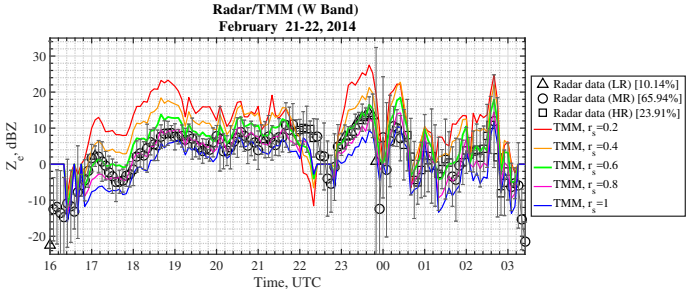

(c)

Figure 10. Same as Figure 8, but for 21/22 February 2014, 16:00-03:24 UTC (LR, MR and HR snowfall in black triangles, points and squares respectively).

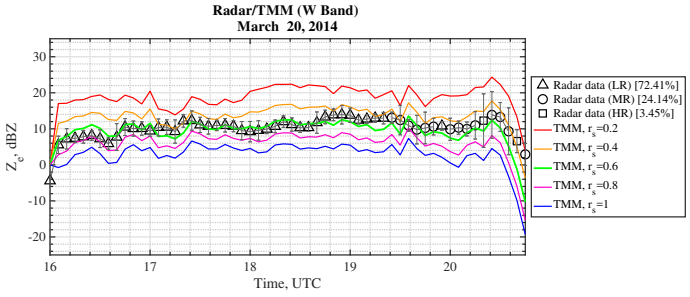

(a)

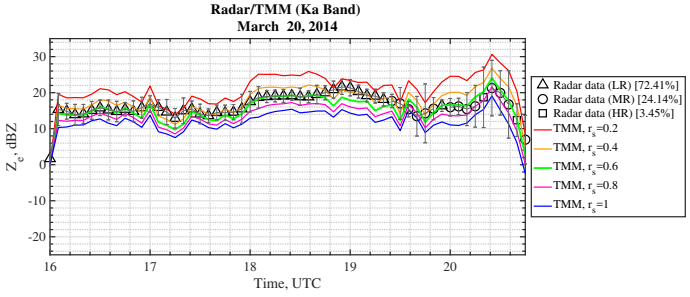

(b)

Figure 11. Same as Figure 8, but for 20 March 2014, 16:00- 20:48 UTC (LR, MR and HR snowfall in black triangles, points and squares respectively). The X band radar data are not available for this time-window.

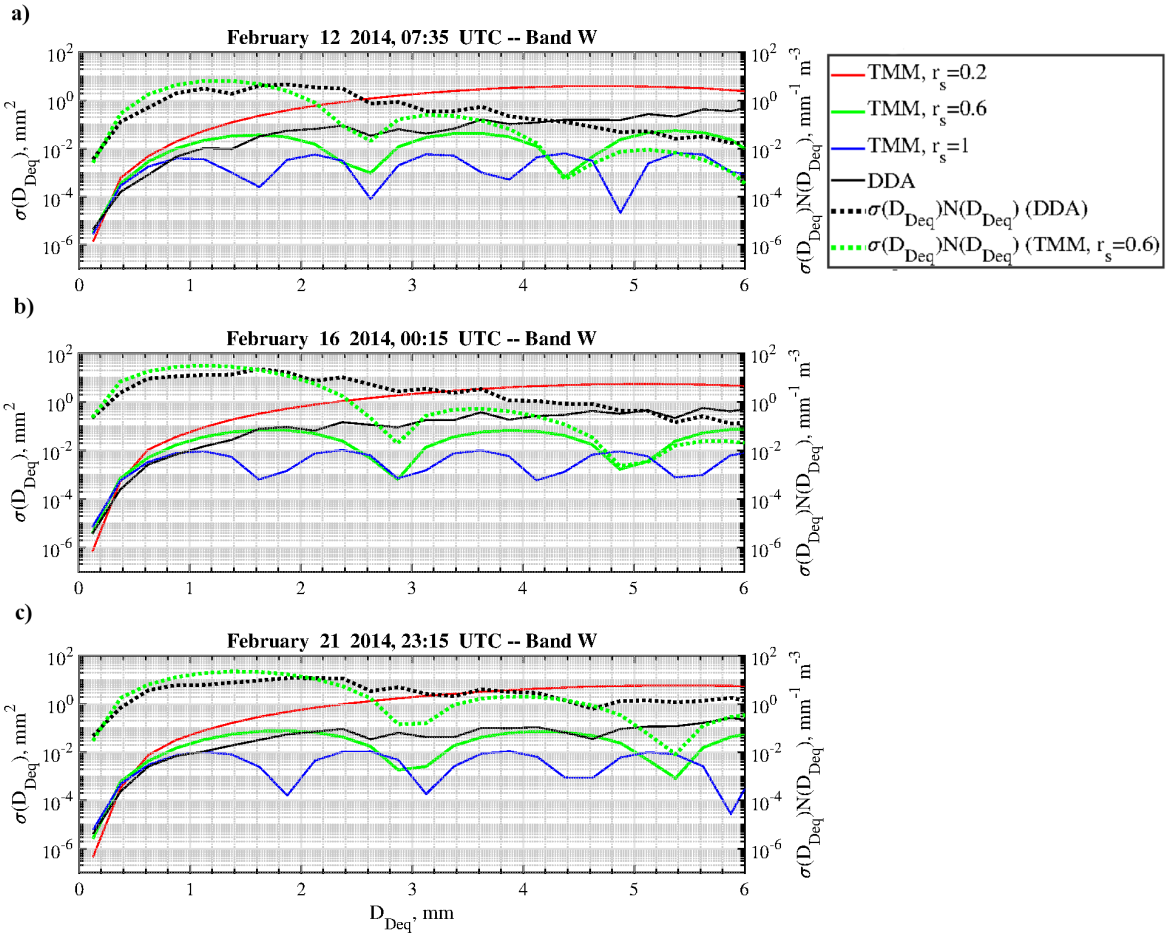

Figure 12. Horizontally-polarized cross section σ, expressed as a function of the diameter disk-equivalent D_{Deq} at W band by comparing DDA computations (black line) and TMM computations (red, green and blue lines, matching $r_s = 0.2$, $r_s = 0.6$ and $r_s = 1$). The product between σ and PIP-derived snowflake size distribution N shows the main contribution of particle size in terms of diameter disk-equivalent for DDA computations (dotted black line) and TMM computations ($r_s = 0.6$, dotted green line).

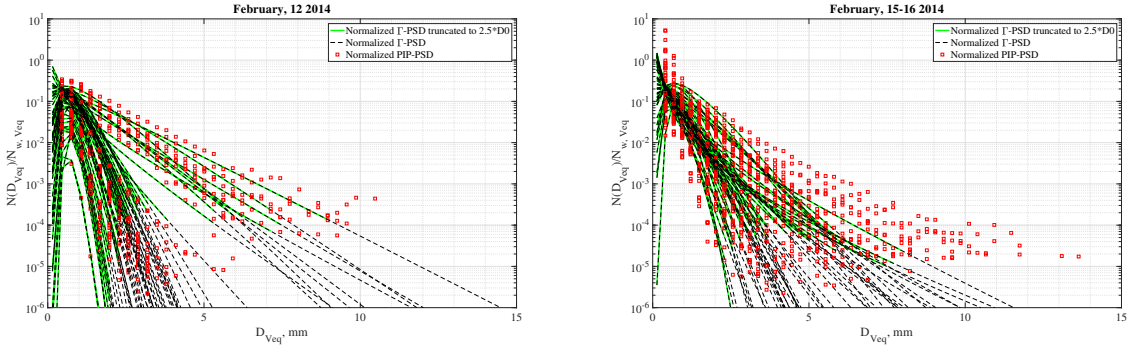

(a) (b)

Figure 13. Figure (a) shows PSD for snowfall case of 12 February 2014 and figure (b) shows PSD for snowfall case of 15/16 February 2014. Red points are representative of the normalized PSD measured by PIP, dashed black line represents the normalized estimated Γ-PSD in Equation (4) and green line is the last one truncated at the maximum value of 2.5 multiplied by the median diameter D_0.